

PAPER

The characteristic radiation of copper $K\beta$ including radiative Auger processes

Recent citations

- [An absolute energy characterisation of scandium K to 2 parts per million](#)
J W Dean *et al*

To cite this article: H A Melia *et al* 2020 *J. Phys. B: At. Mol. Opt. Phys.* **53** 195002

View the [article online](#) for updates and enhancements.



IOP | ebooks™

Bringing together innovative digital publishing with leading authors from the global scientific community.

Start exploring the collection—download the first chapter of every title for free.

The characteristic radiation of copper $K\beta$ including radiative Auger processes

H A Melia, C T Chantler¹ , L F Smale and A J Illig

School of Physics, The University of Melbourne, Melbourne Australia

E-mail: h.melia@student.unimelb.edu.au, chantler@unimelb.edu.au, lucas.smale@gmail.com and ajillig@gmail.com

Received 17 March 2020, revised 15 May 2020

Accepted for publication 7 July 2020

Published 12 August 2020



CrossMark

Abstract

Two characterisations of the Cu $K\beta_{1,3}$ spectrum are developed, which are robust and transferable to other experimental x-ray geometries. By observing and considering the significant contribution of radiative Auger emission to the $K\beta$ profile, we obtain an improved and more robust characterisation. The contribution of the $KM_{2,3}M_{4,5}$ and $KM_{2,3}N_1$ radiative Auger satellites to the $K\beta_{1,3}$ spectrum is measured to be 1.96%. The contribution of radiative Auger emission is often significant and should be included in defining characteristic x-ray spectra. This is a step in the renewed efforts to resolve inconsistencies in characteristic x-ray spectra between theory and common experimental geometries. The spectrum was measured using a rotating anode, monolithic Si channel-cut double-crystal monochromator and backgammon detector. The experimental setup provides insight into the portability of spectral characterisations of x-ray spectra.

Keywords: copper, characteristic radiation, K beta, x-ray spectroscopy, radiative Auger effect

(Some figures may appear in colour only in the online journal)

1. Introduction

Characteristic atomic spectra have been used for decades in the range of scientific applications, including plasma spectroscopy [1, 2], perturbed atomic structure physics [3], laser-produced plasmas [4], the transition from solid to plasma visualized by K -radiation excited by suprathreshold electrons [5], solid state [6] and chemical physics [7]. Knowledge of the precise shape of x-ray spectra is fundamental for applications such as reference spectra in dense plasma atomic physics and in the calibration of energy scales in high accuracy x-ray experiments [8–12]. The study and characterisation of emission spectra gives insight into atomic processes through the empirical fitting of components attributed to electronic transitions. Absolute measurement is a necessary component of characterisation; here the transfer and portability of the spectrum is investigated through a relative measurement. Asymmetries in the line shape have long been explained by the presence of spectator vacancies, created when the photo-electron causes excitation of outer shell electrons, either to the continuum

(shake off) or higher shell (shake up). Contributions to the spectrum created in this way are referred to as shake satellites.

The x-ray spectrum of Cu is the most studied of all the transition metals, with numerous characterisations of the Cu $K\alpha$ spectrum reported over the last century [13–22]. However, there exists very few Cu $K\beta$ characterisations in the literature. The $K\beta$ spectrum is caused by the transition $3p \rightarrow 1s$, this can be further split into the $K\beta_{1,3}$ lines attributed to the hole transitions: $[1s] \rightarrow [3p_{3/2}]$ and $[1s] \rightarrow [3p_{1/2}]$. The energy splitting of the $3p$ subshells is significantly smaller than the $2p$ subshells meaning that the $K\beta$ component lines cannot easily be resolved and so the spectrum appears as an unresolved doublet.

The best current characterisation of the Cu $K\beta$ profile uses a sum of five Lorentzians [18]. The fit shows excellent agreement between data and model. However the physical significance of each Lorentzian is undetermined. This is in contrast to earlier work on the Cu $K\alpha$ spectrum by Deutsch *et al.*, where each Lorentzian is attributed to an electronic transition and therefore to specific atomic processes [17].

Alongside experimental investigations, theoretical investigations give a unique insight into the interaction between

¹ Author to whom any correspondence should be addressed.

Table 1. *KMM* RAE energies according to equation (3). Binding energies from [37, 38].

KM_iM_j	$E(K)$	$E(M_i)$	$E(M_j)$	RAE edge (eV)
KM_1M_1	8978.9	122.5	122.5	8733.9
KM_1M_2	8978.9	122.5	77.3	8779.1
KM_1M_3	8978.9	122.5	75.1	8781.3
$KM_1M_{4,5}$	8978.9	122.5	0	8856.4
KM_2M_2	8978.9	77.3	77.3	8824.3
KM_2M_3	8978.9	77.3	75.1	8826.5
$KM_2M_{4,5}$	8978.9	77.3	0	8901.6
KM_3M_3	8978.9	75.1	75.1	8828.7
$KM_3M_{4,5}$	8978.9	75.1	0	8903.8
$KM_{4,5}M_{4,5}$	8978.9	0	0	8978.9

Table 2. *KMM* RAE energies according to equation (3). Binding energies from [39].

KM_iM_j	$E(K)$	$E(M_i)$	$E(M_j)$	RAE edge (eV)
KM_1M_1	8978.9	119.8	119.8	8739.3
$KM_1M_{2,3}$	8978.9	119.8	73.6	8785.5
$KM_1M_{4,5}$	8978.9	119.8	1.6	8857.5
$KM_{2,3}M_{2,3}$	8978.9	73.6	73.6	8831.7
$KM_{2,3}M_{4,5}$	8978.9	73.6	1.6	8903.7
$KM_{4,5}M_{4,5}$	8978.9	1.6	1.6	8975.7

electrons inside the atom and will be crucial in our continued understanding of intra- and inter-shell electron interaction. Theoretical determinations of the x-ray spectrum of Cu $K\beta$ have been performed with an increasing level of sophistication, driving new theoretical ideas and experimental techniques in an attempt to improve accuracy and understand discrepancies [17, 23, 24].

The spectra of the transition metals have been shown to change with accelerating voltage of the incoming electrons (or photons). X-ray spectra are obtained when the incoming electron has sufficient energy to remove a $1s$ electron in order for a higher shell electron to decay and emit a photon of characteristic energy. This process results in the diagram lines, $K\alpha_{1,2}$ and $K\beta_{1,3}$. The energy required to obtain the diagram lines is the binding energy of the $1s$ electrons, referred to as the threshold. When discussing accelerating voltage two regimes are considered, the near-threshold regime and the well-above-threshold regime. In the well-above-threshold regime we can consider the two electron events as two independent non-interacting processes, modelled by the frozen core or sudden approximation. When considering near threshold energies, the gradual relaxation of the higher shell electrons matter and there is significant wavefunction overlap, often modelled as the adiabatic regime.

The shape of x-ray spectra changes across the two regimes, in the near adiabatic regime we see little evidence of shake satellite lines as the photo-electron does not have sufficient energy to free higher shell electrons. As the energy increases the contribution of the shake satellite lines increases towards saturation. This evolution of the satellite contribution can be approximated using the Thomas model—a time-dependent perturbation calculation [25]—and has been investigated for

various elements experimentally [26–30]. More recently, the evolution of the hyper-satellite structure with excitation energy has also been investigated [31, 32].

1.1. The radiative Auger effect

An important decay mode not considered by Holzer *et al* [18] is the radiative Auger process. This process involves the release of an Auger electron as well as the usual photon emission. However, in this case the available transition energy is shared between the photoelectron and the photon, causing the photon to have a lower energy [33]. The radiative Auger effect (RAE) gives rise to separate satellite lines—radiative Auger satellites (RAS). These satellites must have energy less than the parent line but can be extremely broad features. RAS are defined and named according to the three shells involved—the shell in which the initial vacancy exists, the shell that the decaying electron comes from and the shell the Auger electron is excited from e.g. *KMM*.

In the non-radiative case, the energy of the Auger electron is equal to the characteristic energy less the binding energy of the electron. In the RAE this energy is shared between the Auger electron and the emitted x-ray. Consider the transition KM_iM_j where an aM_i electron fills a vacancy in the K -shell emitting a photon with energy $h\nu$ and an electron, from the M_j -shell, with energy ϵ :

$$h\nu + \epsilon = E(K) - E(M_i) - E(M_j). \quad (1)$$

The RAE edge is defined as the maximum allowed photon energy. This energy corresponds to an Auger electron emitted with zero kinetic energy. In this case the photon receives all the allowed energy and we can write:

$$h\nu = E(K) - E(M_i) - E(M_j) \quad (2)$$

$$E_{\text{RAE edge}} = E(K) - E(M_i) - E(M_j) \quad (3)$$

e.g. for $K\beta_{1,3}$ RAE transitions, this becomes:

$$E_{KM_2M_j \text{ edge}} = E(K\beta_1) - E(M_j) \quad (4)$$

$$E_{KM_3M_j \text{ edge}} = E(K\beta_3) - E(M_j). \quad (5)$$

Associated with the RAE edge is the energy corresponding to the maxima in intensity, E_m . For a symmetric function this will be the peak centroid. E_m will always be less than the RAE edge energy. For symmetric RAE fitting functionals the difference can be large. However, we expect the transition probability to be at a maximum when the electron is emitted with zero kinetic energy and to then drop off slowly with an increasing electron kinetic energy, ϵ [34]. This would imply $E_{\text{RAE edge}} \approx E_m$ which cannot be the case for a broad symmetric function. Experimentally the difference between E_m and the RAE edge has been reported to be significant [35, 36].

Table 1 shows the RAE edge energy for each of the Cu *KMM* transitions obtained using equation (3). Binding energies for the K -shell have been taken from [37] and all other subshells from [38]. Table 2 uses the binding energies from [39]. The difference in binding energies leads to RAE edge

Table 3. The *KMM* RAE percentage contribution to the $K\beta_{1,3}$ spectrum for various elements as reported. The functional form used for the RAE is listed.

Element	Z	<i>KMM</i> (%)	Functional form	Reference
Mg	12	20(5)	Gaussian	Limandri <i>et al</i> [36]
Al	13	22(4)	Gaussian	Limandri <i>et al</i> [36]
Si	14	42.5(28)	Gaussian	Limandri <i>et al</i> [36]
Ca	20	3.14(47)	Not modelled ^a	Budnar <i>et al</i> [35]
Ca	20	4.3(15)	3 Gaussians	Kavcic <i>et al</i> [65]
Ca	20	3.26(15)	Exponential \otimes Gaussian ^b	Baptista [68]
Sc	21	10.7(1)	1–4 Gaussians	Cipolla [70]
Sc	21	1.39(8)	Gaussian	Limandri <i>et al</i> [36]
Ti	22	2.44(37)	Not modelled ^a	Budnar <i>et al</i> [35]
Ti	22	2.6(2)	Left sided Gaussian	Bé <i>et al</i> [64]
Ti	22	3.0(11)	3 Gaussians	Kavcic <i>et al</i> [65]
Ti	22	8.6(2)	1–4 Gaussians	Cipolla [70]
Ti	22	2.62	Exponential \otimes Gaussian ^b	Baptista [68]
Ti	22	1.12(2)	Gaussian	Limandri <i>et al</i> [36]
V	23	2.3	Not modelled ^c	Servomaa <i>et al</i> [71]
V	23	6.4(2)	Left sided Gaussian	Bé <i>et al</i> [64]
V	23	3.8(1)	1–4 Gaussians	Cipolla [70]
Cr	24	2.0	Not modelled ^c	Servomaa <i>et al</i> [71]
Cr	24	2.91(58)	Not modelled ^a	Budnar <i>et al</i> [35]
Cr	24	3.2(1)	Left sided Gaussian	Bé <i>et al</i> [64]
Cr	24	2.98	Exponential \otimes Gaussian ^b	Baptista [68]
Cr	24	13(1)	Gaussian	Limandri <i>et al</i> [36]
Mn	25	2.4	Not modelled ^c	Servomaa <i>et al</i> [71]
Mn	25	2.5(1)	Left sided Gaussian	Bé <i>et al</i> [64]
Fe	26	1.6	Not modelled ^c	Servomaa <i>et al</i> [71]
Fe	26	2.5(1.4)	3 Gaussians	Kavcic <i>et al</i> [65]
Fe	26	3.5(4)	Left sided Gaussian	Bé <i>et al</i> [64]
Fe	26	3.8(1)	1–4 Gaussians	Cipolla [70]
Fe	26	17.4(8)	Gaussian	Limandri <i>et al</i> [36]
Co	27	1.4	Not modelled ^c	Keski-Rahkonen <i>et al</i> [45]
Co	27	6.8(2)	Left sided Gaussian	Bé <i>et al</i> [64]
Co	27	3.79(4)	6 Gaussians	Seetharami <i>et al</i> [44]
Ni	28	1.2	Not modelled ^c	Keski-Rahkonen <i>et al</i> [45]
Ni	28	1.7(1)	Left sided Gaussian	Bé <i>et al</i> [64]
Ni	28	7.6(4)	Gaussian	Limandri <i>et al</i> [36]
Ni	28	3.43(3)	6 Gaussians	Seetharami <i>et al</i> [44]
Cu	29	1.1	Not modelled ^c	Keski-Rahkonen <i>et al</i> [45]
Cu	29	1.2(1)	Left sided Gaussian	Bé <i>et al</i> [64]
Cu	29	2.40(3)	1–4 Gaussian	Cipolla [70]
Cu	29	3.349(171)	—	Cengiz <i>et al</i> [72]
Cu	29	3.24(3)	6 Gaussians	Seetharami <i>et al</i> [44]
Zn	30	1.4	Not modelled ^c	Keski-Rahkonen <i>et al</i> [45]
Zn	30	3.7(3)	1–4 Gaussians	Cipolla [70]
Zn	30	6.1(4)	Gaussian	Limandri <i>et al</i> [36]
Zn	30	3.05(3)	6 Gaussians	Seetharami <i>et al</i> [44]
Ga	31	2.91(3)	6 Gaussians	Seetharami <i>et al</i> [44]
Ge	32	4.1(4)	1–4 Gaussians	Cipolla [70]
Mo	42	1.14(9)	1–4 Voigts	Herren <i>et al</i> [66]
Ru	44	1.36(9)	1–4 Voigts	Herren <i>et al</i> [66]
Pd	46	0.99(8)	1–4 Voigts	Herren <i>et al</i> [66]
Cd	48	0.46(7)	1–4 Voigts	Herren <i>et al</i> [66]
Sn	50	0.36(5)	1–4 Voigts	Herren <i>et al</i> [66]

^aObtained as the difference between the fit and the measured spectrum.^bRAE probabilities were calculated theoretically. RAE structure was modelled as an exponential convoluted with a Gaussian; \otimes convolution.^cOnly includes contributions from the $3s$ and $3p$ electrons. Obtained as the difference between the fit and the measured spectrum.

energy differences $\approx 0\text{--}6$ eV. Unfortunately the x-ray tabulations of [40] do not include M -shell binding energies. However, the K shell energies are consistent with [39] within 1 eV (8980.476(20) eV from direct measurement of the extremum of the derivative spectrum [41]; 8980.5(10) eV derived using outer shell binding energies). Whilst [41] is an absolute measurement and perhaps the best currently available, it is dependent upon a possible pre-edge bound-bound structure and is dependent upon experimental resolution and temperature. Hence, the uncertainty in applying the derivative definition to the experimental measurement and calibration is a larger uncertainty than the original measurement.

Hence, as a rough estimate, table 1 has an error or uncertainty of 2.5 eV for the K -edge; and something similar for the M_1 , M_2 , M_3 and $M_{4,5}$ edges. Transparently the $M_{4,5}$ edges are bound and not at the continuum so this error is of order 1.6 eV. Conversely, table 2 has an error or uncertainty of approximately 1.6 eV for the K -edge; perhaps 1–2 eV for M_1 ; perhaps 2.2 eV for M_2 or M_3 given that they are non-degenerate; and maybe less than 1 eV for $M_{4,5}$. The net result is that table 2 is expected to be more accurate yet still have an uncertainty of approximately 3 eV for the RAE edge energies. The angular momentum coupling strongly impacts the KM_1M_j and KM_2M_j energies [34, 42–44], and for Cu the main separation of the doublet is predicted to be 7.5 eV [45].

KMN Auger profiles exist, yet the small or negligible binding energy of the N -shell electron means that their edge will coincide with the relevant $K\beta$ transition. In our current spectra, any KM_1M_j RAS will lie below the spectral region observed, as will any $KM_{2,3}M_{2,3}$ RAS; and any $KM_{4,5}M_{4,5}$ RAS and the $K\beta_{2,5}$ spectral line from $KM_{4,5}$ will lie above the energy range of the spectrum although one might see a small background tail function. Hence in the spectral region of interest, the $KM_{2,3}M_{4,5}$ RAS, a narrow doublet will dominate the RAS observed in the data.

Kawai *et al*, and other authors, have studied the relationship between an RAE satellite structure and x-ray absorption fine structure (XAFS) [46–49] and used this to measure an XAFS-like structure in the RAE spectra for various elements including Na, Si, Al and Mg [50–53]. This relationship has also been studied theoretically using molecular orbital models and one-step quantum mechanics [54, 55]. These ideas promote the potential of new techniques; a deeper understanding of RAE processes and structure will help realise this potential.

The value of modelling x-ray spectra using analytical functionals is given by the strength of conclusions that can be drawn about the atomic processes involved in creating the spectra. In 1974 the $K\alpha/K\beta$ transition ratio, obtained through theoretical single potential relativistic Hartree–Slater calculations [56–58], were compared to experimental results, obtained through x-ray spectroscopy and fitting functions, over a range of atomic numbers ($12 < Z < 100$) [59]. Across all Z , the theoretical predictions underestimated the ratio obtained through the experiment. Figure 2 of Berenyi *et al* [60] shows that this discrepancy persists when comparing relativistic Hartree–Fock calculations [61], including the exchange effect of the nonzero overlap between subshells, with experimental

results. It is troubling that theory and experiment disagreed across the literature for the majority of the periodic table, suggesting that some key pieces of physics were missing. In 1986 this discrepancy was investigated through modelling RAE with a Gaussian [62]. This has been repeated with some success [63, 64]. This highlighted the need for inclusion of RAE, yet the shape of the RAE satellites are still unknown and continue to be overlooked in many investigations.

In the literature there have been several approaches to implementing the shape of the RAS. One method is to examine the residual of fits that make no attempt to model it. This has been done for specific elements and shows the RAS to have broad features on the low energy side of the main lines [34, 35]. Another method is to use one or more Gaussian or Voigt functions to represent each RAE peak [36, 62, 65, 66]. Such functionals do not match the expected antisymmetric shape. Modelling the RAS using similar functionals as discrete peaks may lead to large correlations between fitting parameters. Bé *et al* [64] used ‘Gaussians with left-sided tails’ to model the RAE to account for antisymmetry empirically. Although this fits better than Gaussians, residuals remain on the low energy side of the main peaks, in common with [67]. Alternatively the RAS have been modelled using more exotic analytic functions, the basis of which are varied. Baptista *et al* model the RAS as exponentials convoluted with a Gaussian. This represents some asymmetry; however their choice of shape is not justified [68].

Enkisch *et al* [26] have modelled the KMN RAS in the Cu $K\beta$ spectrum using the function:

$$I_{\text{RAS}}(E) = \frac{Ie^{d(E-E_0)}}{e^{(E-E_0)/w} + 1} \quad (6)$$

where d is the decay factor, w is the half width at half maximum of the parent line ($K\beta_{1,3}$), E_0 is the edge energy and I is an amplitude factor. The decay factor d accounts for the low energy tail of the RAS whilst the Fermi function, characterised by w , provides the steeper drop on the high energy side. Including this function yields modest residuals on the low energy shoulder of the $K\beta_{1,3}$ spectrum.

The contribution of the RAE to the Cu $K\beta_{1,3}$ spectrum was first estimated by Keski-Rahkonen, giving a result of 1.1%. This was estimated by looking at the integrated intensity of the residuals compared with the dominant $K\beta_{1,3}$ line, rather than modelling the component and finding the integrated intensity [45]. Limandri *et al* modelled the RAS in the $K\beta$ x-ray spectra using a Gaussian function for several elements excluding Cu, obtaining a contribution to the total spectrum ranging from 1.12% for Ti, to 42.5% for Si [36]. Some of these are infeasibly high due to the RAE Gaussian stealing intensity from the purely radiative decay processes in the spectrum. Modelling the KMM RAS across elements $Z = 22\text{--}29$ as an asymmetric Gaussian produced contributions as small as 1.2(1)% for Cu and as large as 6.8(2)% for Co [64]. Table 3 shows the KMM contribution to the $K\beta_{1,3}$ spectrum found in the literature for various elements. Also shown is the method for estimating the contribution, from fitting or counting residuals. There are large discrepancies between percentages even when using the same modelling function. The contribution does appear

to decrease with Z as expected. Theoretical predictions are given by Scofield for five elements: Ar, Fe, Kr, Zr and Xe. For comparison, interpolation has often been used to find the value for other elements; yet it is known that these probabilities are strongly discontinuous functions with atomic number Z [69].

Although shake-satellites and RAS both contribute to the asymmetry of the spectrum, they do so in fundamentally different ways. The shake-satellites are non-degenerate (discrete) because of the spectator vacancy during the emission of the measured x-ray. This vacancy is created by a sudden change in electron configuration when the initial $1s$ electron is removed. The energy of the emitted electron has no influence on the energy of the measured x-ray, however the energy of the bombarding particles will affect the contribution of the shake satellites to the spectrum.

Conversely, RAS are created by the change in electron configuration when the higher shell electron ($3p$ in the $K\beta$ case) decays. In this case, the energy of the emitted x-ray is shared with the electron but the contribution to the spectrum is not affected by the energy of incident particles [34].

2. Experimental setup

A MacScience SRA M18XH1 water-cooled rotating anode was used to generate the Cu $K\beta$ spectrum. The spectrum was measured using a backgammon type multi-wire gas proportional counter. A 10 mA current was passed through a tungsten filament producing a stream of electrons incidents on a Cu anode at 20 kV. X-rays exited the rotating anode through a 1 mm slit. The beam was diffracted using a monolithic Si(111) channel-cut crystal, attenuated using aluminum foils and then projected onto the detector face. Full details of the experiment, detector and initial processing steps are described in [73].

3. Deconvolution

The natural line shape of x-ray spectra has been modelled well in the past using the sum of Lorentzians [14]. In all experiments there will be some sources of inhomogeneous broadening that will need to be removed, usually through deconvolution, or including the fit by use of Voigt functions. In the second case, if the fit to the data is satisfactory, setting the Gaussian parameter to zero will result in the natural line shape that would otherwise be obtained through deconvolution. We have performed deconvolution successfully; however, it requires uniform broadening across the energy range and accurate knowledge of the instrument function, possibly obtained through a detailed Monte Carlo simulation.

The data obtained here has significant inhomogeneous broadening. To remove this, a deconvolution was performed through fitting the data to the model function shown in equation (A.1) with parameters from [18], setting the common broadening parameter to zero and then adding the residuals. The accuracy of this approximation can be tested. The goodness of fit, the reduced chi-squared, χ_r^2 is 1.78. The result

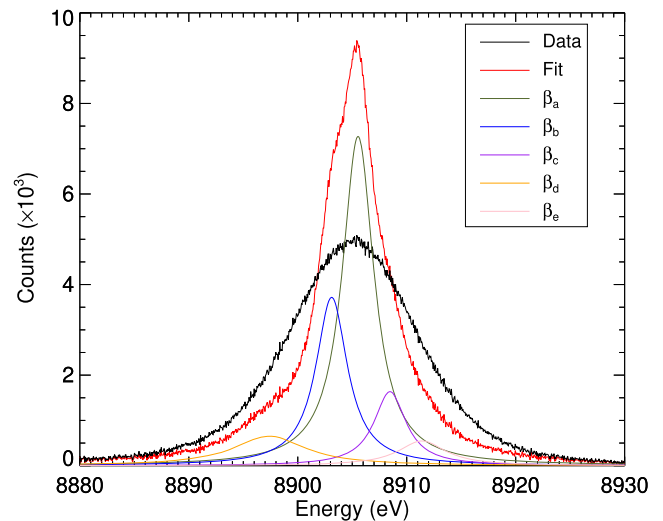


Figure 1. The black line shows the raw spectrum, including Gaussian broadening. The red line shows the deconvolved data, modelled using the best available $K\beta$ parameterisation [18] and yielding $\chi_r^2 = 1.78$. Hence our data is fully consistent with [18] and deconvolving provides a good approximation to the natural line shape.

in figure 1, is well-fitted with residuals similar in shape and magnitude to [18]. The Gaussian broadening removed had a full-width half-maximum $fwhm$ of 10.02 eV. This model also allowed for common homogeneous broadening, through an additional common Lorentzian parameter; for this data the additional instrument functional Lorentzian broadening was found to be zero. This procedure also determined the energy scale of our data.

4. Fitting

We then refitted the spectrum to search for variation of parameters and robustness. A Levenberg–Marquardt least-squares process [74] fitted the model function to the deconvolved data. Each parameter was left free, yielding parameters given in table 4. The energy scale has been calibrated in the deconvolution process. Figure 2 shows the five Lorentzian fit and residuals. The model function is consistent with the data with only a slight improvement on the parameters of [18], reflected in the reduction of χ_r^2 from 1.78 using the characterisation of [18], to 1.76 for our characterisation.

The validity of our deconvolution method can be tested by applying our characterisation, obtained from the deconvolved data, to the original data using the sum of five Voigt profiles (figure 3, $\chi_r^2 = 1.76$). This again provides a smaller χ_r^2 than when we use [18], so the deconvolution process appears valid.

5. RAS consideration

The origin of the low energy β_d contribution (elsewhere called $K\beta'$ [17, 23, 75–77]) is the least clear feature in the spectrum. Over the years several explanations of this feature, found in all the transition metals, have been considered leading to a

Table 4. Parameters obtained after fitting the deconvolved data. Numbers in parentheses are one standard error uncertainties. χ_r^2 was 1.76. The lower panel shows the characterisation of [18], for comparison.

This work			
Peak	Energy (eV)	FWHM (eV)	Integrated intensity (%)
$K\beta_a$	8905.519(11)	3.420(74)	46.92(180)
$K\beta_b$	8903.101(26)	3.462(71)	24.71(108)
$K\beta_c$	8908.432(46)	3.821(264)	12.83(156)
$K\beta_d$	8897.661(89)	8.339(141)	10.62(29)
$K\beta_e$	8911.482(195)	5.419(230)	04.92(73)

Hölzer <i>et al</i> [18]			
Peak	Energy (eV)	FWHM (eV)	Integrated intensity (%)
$K\beta_a$	8905.532(2)	3.52(1)	48.5(2)
$K\beta_b$	8903.109(10)	3.52(1)	24.8(2)
$K\beta_c$	8908.462(20)	3.55(3)	11.0(2)
$K\beta_d$	8897.387(50)	8.08(8)	10.0(2)
$K\beta_e$	8911.393(57)	5.31(8)	5.5(2)

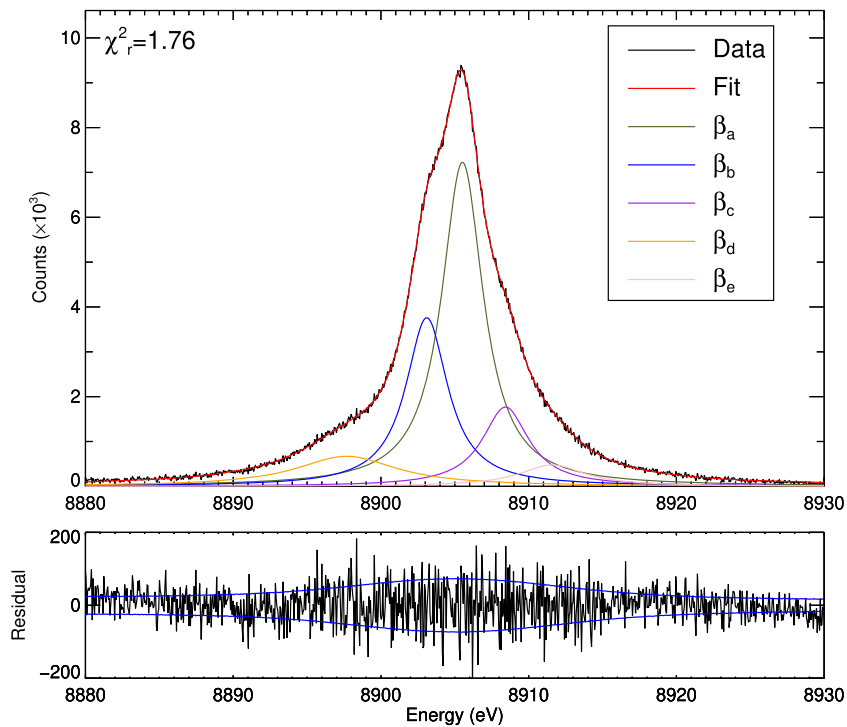


Figure 2. The five Lorentzian sum fit to the deconvolved data improves upon the fit obtained using the parameters from [18]. Parameters of each component are shown in table 4. The panel below shows the residuals of the fit (in black) and one standard error envelope (blue line). Residuals are well-behaved but also show some small structure.

range of investigations over several branches of physics and chemistry. The most likely explanation is the $3d$ spectator hole transitions seen in Pham *et al* [24, figure 3] and Deutsch *et al* [17, figure 10]. However, both show significant residuals around 8897 eV indicating that some other process may cause the peak at this energy. Other explanations of this line include an exchange interaction between the $3p$ hole and the incomplete $3d$ shell [75]. However, this explanation implies that the

line should be absent in the Cu spectrum as here the $3d$ shell is full [78]. Another explanation considers the $K\beta_{1,3}$ photon losing energy through plasmon oscillation in the conduction band and thus creating a low energy satellite [76, 79]. Deutsch *et al* [17] suggested that in the presence of $3d$ hole states an exchange interaction between $3d$ holes and $2p$ hole in the final state was responsible. However, some proportion of the line can be explained by RAS that occur when the atom is excited

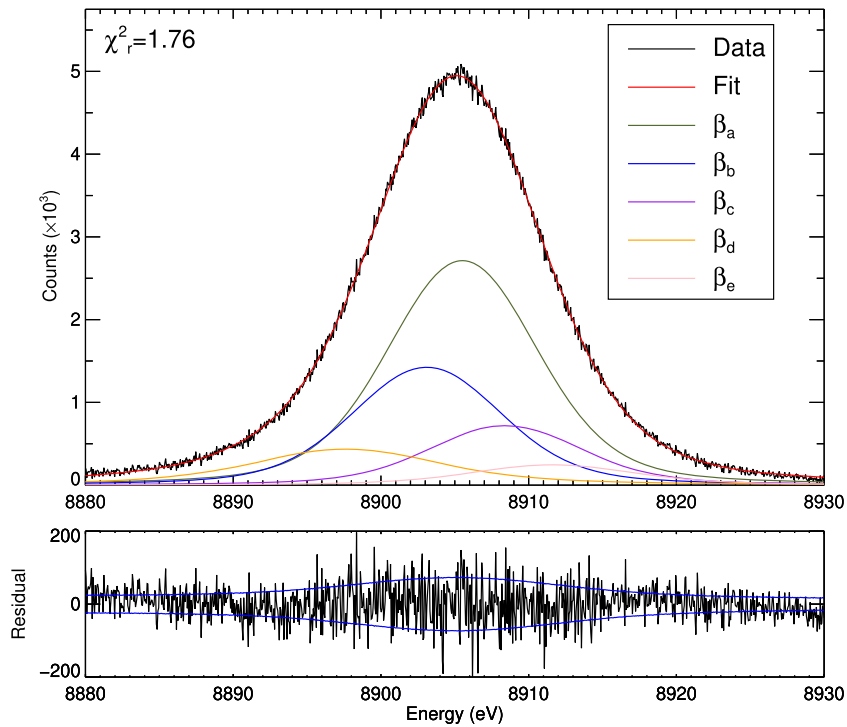


Figure 3. The five Voigt sum fit to the raw data, using the parameters obtained from fitting the deconvolved data (figure 2). The fit produces $\chi_r^2 = 1.76$: our parameters fit both the raw and deconvolved spectra slightly better than [18].

(shaken) by the $3p$ electron that fills the $1s$ vacancy. Then the emitted photon transfers some of its energy to the Auger electron, meaning that these satellites will always lie on the low energy side of the diagram lines. They can be extremely broad features, extending over hundreds of eV [26]. RAS are one explanation of the residuals around 8897 eV shown in theoretical calculations by Pham *et al* [24, figure 3] and Deutsch *et al* [17, figure 10].

The contribution of the *KMM* RAS to the Cu $K\beta$ spectrum have been shown to be on the order of 1–3% following table 3 [44, 45, 61, 64, 70]. Tables 1 and 2 show the RAE edge for each of the *KMM* RA transitions. The only two RAS we expect to be present in our spectrum are the $KM_{2,3}M_{4,5}$ and $KM_{2,3}N_1$, with edge energies within 8901–8906 eV. Interestingly, none of the RAE contribution to the Cu $K\beta$ spectrum previously reported have been attributed to *KMN* transitions [44, 45, 64, 70]. Because the $3p_{1/2}$ and $3p_{3/2}$ levels are close in energy it is common practice in the literature to model the $KM_{2,3}M_j$ structure with one analytic function, rather than fitting KM_2M_j and KM_3M_j separately or rather than fitting the eigenvalues for the angular momenta for the coupled electron wavefunctions.

Here we model the inclusion of RAS in the Cu $K\beta$ spectrum. The entire RAS structure was modelled using equation (6). The intensity was left free, w was set to the half width at half maximum of $K\beta_{1,3}$ and d was tied following [26]. The edge energy, E_0 , could be tied to a theoretical value from the binding energies of the subshells (equation (3)) or left as a free parameter. The fit is undefined if several RAS are modelled simultaneously in this spectrum. Leaving the edge energy as a free parameter gave a value of 8906.0 eV (table 5), slightly

Table 5. χ_r^2 for a given E_0 . For all columns except the first E_0 was fixed.

	Free	Enkisch <i>et al</i> [26]	$KM_{2,3}N$	$KM_3M_{4,5}$	$KM_2M_{4,5}$
E_0	8906.0	8900.8	8905.5	8903.8	8901.7
χ_r^2	1.583	1.582	1.582	1.582	1.582

higher than using equation (3) yet with a very large uncertainty; this change had no significant effect on the other fitting parameters or χ_r^2 .

Figure 4 shows the deconvolved spectra fitted using five Lorentzians and the RAS modelled as described above. The parameters, in table 6, show a very significant divergence from the earlier fit, especially for the integrated intensity of the satellite lines. Although each of the RAS, $KM_2M_{4,5}$, $KM_3M_{4,5}$ and $KM_{2,3}N_1$, have their own edge energies and origin, here they were modelled as a single RAS. The resolution and the narrow energy separations implied that the RAS were not separately identifiable and became heavily correlated.

The angular momentum coupling of the two holes will also affect the energies of the radiative Auger photon—resulting in a further splitting of the RAS. For the $KM_{2,3}M_{4,5}$ transitions there are six ways to couple. Although little work has been done on the momentum coupling of the *KMM* transition we can consider the work on *LMM* transitions for inspiration. Experimentally in the *LMM* transitions the 1F and 3D lines appear dominant and separated by roughly 7.5 eV [80, 81]. Modelling each of these angular momentum coupling states individually in our spectra gave no improvement to using a single RAS function. The individual states could not be resolved. Distinguishing these lines is more feasible when investigating

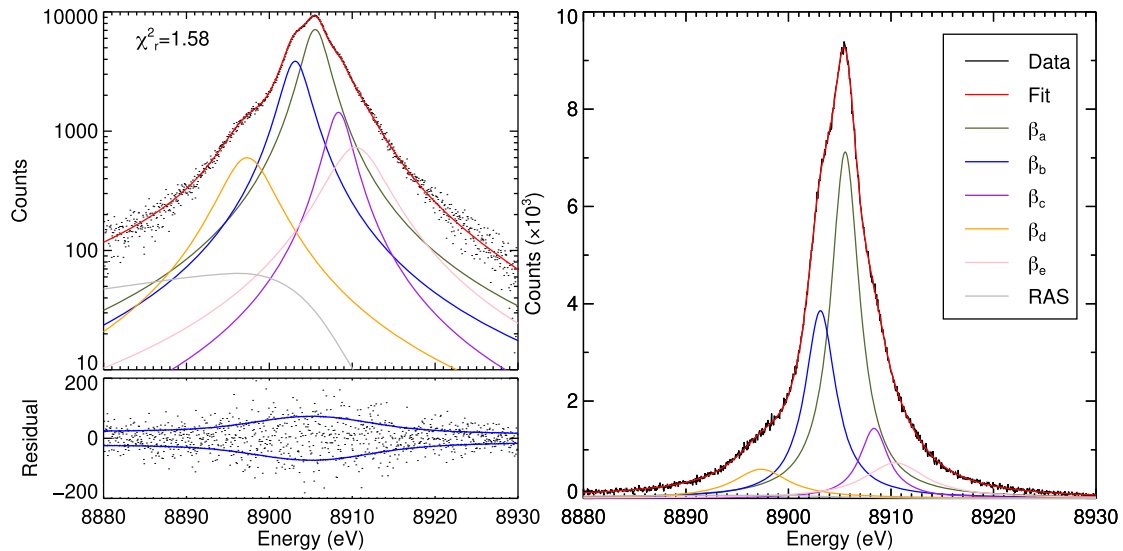


Figure 4. The right panel shows five Lorentzian fit now including a contribution from RAS, modelled using equation (6). χ_r^2 is reduced to 1.58 by including RAS, indicating the significance for obtaining transferable parameterisations. The left panel shows the same fit on a log scale to emphasise the RAS. The lower left box shows the residuals of the fit.

Table 6. The parameters of the fit with the inclusion of the RAS satellite. Numbers in parentheses are one standard error uncertainties. $\chi_r^2 = 1.58$. I_{int} is the integrated intensity to the total spectrum across the fitted energy range. I_{int}^* is the integrated intensity calculated over all energies. The only significant difference between these two columns relates to the RAS profile which according to the functional form used has a very large tail and so contributes much intensity outside the fitting range. The RAS parameters d and w were defined in accordance with [26]. w is the half width at half max of the $K\beta_{1,3}$ line. The $KM_3M_{4,5}E_0$ was chosen for the dominant RAE component on the basis of statistical degeneracy (table 5).

Peak	Energy (eV)	FWHM (eV)	I_{int} (%)	I_{int}^* (%)	
$K\beta_a$	8905.535(12)	3.392(76)	45.84(177)	44.33(172)	
$K\beta_b$	8903.118(28)	3.623(72)	26.43(117)	25.64(114)	
$K\beta_c$	8908.347(49)	3.360(335)	09.17(195)	8.87(189)	
$K\beta_d$	8897.325(74)	6.571(207)	07.09(31)	7.22(31)	
$K\beta_e$	8910.430(360)	7.268(218)	09.52(164)	9.75(168)	
	E_0 (eV)	w (eV)	I_{int} (%)	I_{int}^* (%)	d (eV ⁻¹)
RAS	8903.8	2.96	1.96(15)	4.19(31)	0.023

RAS further away from the dominant $K\beta$ lines, however these features do not affect the $K\beta_{1,3}$ characterisation.

As discussed, some authors have approximated the RAS with symmetric functions—Gaussians or Voigts. With our data these symmetric options resulted in much worse fits and higher χ_r^2 as expected, compared with using equation (6).

The functional form for the shape of RAS in x-ray spectra is not clear in the literature. The function suggested by Enkisch *et al* [26] was chosen in this research primarily because it provided the necessary antisymmetric shape and consistently produced fits with lower χ_r^2 when compared to Gaussian or Voigt profiles. Furthermore, the simplicity of the function means only two parameters have to be added to the fitting function. Table 3 demonstrates the lack of antisymmetric alternatives.

6. Analysis

The two prominent peaks (β_a and β_b) can evidently be identified by the diagram lines, $K\beta_1$ and $K\beta_3$, resulting from transitions $[1s] \rightarrow [3p_{3/2}]$ and $[1s] \rightarrow [3p_{1/2}]$. The other three spectral components ($\beta_{c,d,e}$) are expected to be dominated by spectator vacancies. This interpretation yields a satellite line contribution of 0.287 or 28.7%, in good agreement with the results of Deutsch *et al*, obtained through the empirical fitting of single and double crystal spectroscopy data [17], and with multi-configurational Dirac–Fock calculations applied to the same data [82, 83].

Earlier work focussed on the $3d$ hole transitions, $[1s3d] \rightarrow [3p3d]$ yielding a $3d$ shake probability $\approx 30\%$. However, the

Table 7. Difference in parameters of our five Lorentzian fit from [18]. The lower panel shows the difference as a fraction of the sum of 1σ (standard error) uncertainties.

Difference			
Component	Energy (eV)	FWHM (eV)	Area (%)
$K\beta_a$	-0.014	-0.010	-1.584
$K\beta_b$	-0.008	-0.058	-0.091
$K\beta_c$	-0.030	0.271	0.827
$K\beta_d$	0.274	0.259	0.628
$K\beta_e$	0.201	0.109	-0.580

Difference w.r.t. parameter standard errors			
Component	Energy (eV)	FWHM (eV)	Area (%)
$K\beta_a$	-1.010σ	-1.187σ	-0.778σ
$K\beta_b$	-0.223σ	-0.716σ	-0.071σ
$K\beta_c$	0.458σ	0.923σ	1.030σ
$K\beta_d$	1.973σ	1.173σ	1.342σ
$K\beta_e$	0.794σ	0.351σ	-0.613σ

latest theoretical calculations indicate a lower shake probability for the $3d$ shells and that other spectator vacancies make a significant contribution. Pham *et al* use multi-configurational Dirac–Hartree–Fock to predict the contribution from $4s$ and $3p$ holes as 12.43% and 7.74%, respectively [24]. The $4s$ satellite structure is almost identical in energy to the diagram lines, so any contribution from the $4s$ satellite structure will be included in the fitted β_a and β_b components.

Although the fit here is empirical, we can make a preliminary discussion on the origin of each of the lines by comparing to [24]. The ‘stick diagrams’ [24, figure 2] show the structure of each of the hole satellites as determined using MCDF. Comparing this to figure 4 indicates that our $K\beta_c$ component is likely made up of several different hole transitions: $[1s3d] \rightarrow [3p3d]$, $[1s3p] \rightarrow [3p^2]$ and to a lesser extent $[1s3d^2] \rightarrow [3p3d^2]$. The $K\beta_d$ component lines up well with the low energy $3s$ contribution caused by the $[1s3s_{1/2}] \rightarrow [3p3s_{1/2}]$ transitions. However according to the *ab initio* probabilities calculated by Pham *et al* this transition is much too weak to produce a line as strong as the $K\beta_d$ line. Alternatively our $K\beta_d$ line may be caused by a combination of the low energy $3d$ and $3d^2$ hole transitions, as well the RAE. Lastly, the high energy $K\beta_e$ component is created through high energy $3d$ and $3d^2$ hole transitions. We expect the widths of each of the components, especially $K\beta_d$ and $K\beta_e$, to be larger than the natural line widths of the transitions because there are multiple transitions contributing to each Lorentzian. This explains the widths of $K\beta_{a,b}$ being slightly larger than theoretical values of [84]. The widths of the other components are significantly larger than that of an individual theoretical transition width because these components need to account for multiple complex satellite structures and in some cases the structure of double satellite transitions [24].

Our characterisation is generally consistent with that by Holzer *et al* [18]. The largest discrepancies, almost 2σ , are in the parameters of the low energy β_d satellite. The shift in each parameter is shown in table 7.

Despite Cu being one of the most investigated of all x-ray spectra there exists very few full characterisations or measures of the *fwhm* of the Cu $K\beta$ spectrum in the literature. The *fwhm* of our $K\beta_{1,3}$ spectrum was measured to be 5.913(1) eV similar to that found by Holzer *et al* at 5.92 eV. Earlier *fwhm* measurements were made by Obert and Bearden [85] and by Edamoto (using x-units) [86], who report *fwhms* of 6.01 eV and break 6.49 eV, respectively.

A comparison of tables 4 and 6 show significant differences, especially in the satellite parameters, upon the inclusion of the RAS profile. The reduction in χ_r^2 indicates that the RAS feature makes an improvement, and is a real and important contributor in explaining the shape of x-ray spectra and their transferability. The estimation of significance is particularly presented by the *F*-test, which depends on the change of χ^2 rather than χ_r^2 . In this case $\Delta\chi^2$ is 173, so quite significant. The formal *F* test can be used to determine whether this change is significant. Consider the *F* statistic,

$$F = \frac{\Delta\chi^2 N_{\text{dof}}}{\chi_r^2 \Delta p} \quad (7)$$

where N_{dof} is the number of degrees of freedom in the model we are testing (in our case the RAE model) and Δp is the difference in the number of parameters of the two models. In order for the *F*-test to pass, the *F* statistic must be greater than the critical value of the *F*-distribution for some level of confidence, e.g. 95%, $\alpha = 0.05$. This critical value takes into account the degrees of freedom, Δp , N_{dof} through the parameters of the *F*-distribution (often labelled ν_1 and ν_2). For our data the *F* statistic is far greater than the critical value $F \approx 56 \gg F_{\nu_1, \nu_2, 0.01} = 6.66$, meaning we can say with $> 99\%$ confidence that the model that includes a functional form for the RAE is significantly better than the five Lorentzian sum model.

The strength of the empirical fitting of Lorentzians or Voigts to the x-ray spectra is the link with electronic processes, such as shake and radiative Auger processes. The literature has not had great success in attributing specific atomic processes to each $K\beta$ component—as we have done with Cu $K\alpha$. Nonetheless, by correctly attributing some of what has long been called $K\beta'$ to RAS we are a step closer to the realization of such a characterisation. This task is made difficult for $K\beta$ spectra by the experimental resolution and the significant overlap between components.

Theoretical predictions suggest that the RAE contribution to the $K\beta$ spectrum are roughly an order of magnitude larger than in the $K\alpha$ spectra [61], so investigation of the RAS functional form is ideal in the $K\beta$ spectrum. The exact shape of the RAS contribution is currently ill-defined. Investigations into the structure are ongoing and important.

7. Conclusion

The five Lorentzian fit provides an improved alternative, reflected in a lower χ_r^2 , to the characterisation given by [18] while also displaying the robustness of the characterisation across experimental geometries. Residuals around the $K\beta_d$ line continues to show the largest inconsistencies and leads us to the second characterisation. Despite the RAE being a significant atomic process, RAS have often been neglected

when modelling x-ray spectra, leading to errors in transferability of reference characterisations and the conclusions drawn from empirical fits. Here we demonstrate that modelling the RAS with an analytic function alters the other components of the characterisation quite significantly. Modelling the RAS offers a superior fit, yielding a lower χ_r^2 , and explaining long standing residuals in Cu $K\beta_{1,3}$ fits around the troublesome low energy shoulder. More work on the precise shape and functional form of RAS satellites is required, so that these contributions can be well understood and documented in x-ray characterisations.

Acknowledgments

We acknowledge A T Payne for his part in the development of the Backgammon detector technology and of the data acquisition. We acknowledge the group of X-ray Optics and Synchrotron Science at the School of Physics.

Appendix A. Fitting function

The function used to model the spectrum is the sum of five Voigt functions and background parameters $B(E)$:

$$f(E) = \sum_{i=1}^5 V_i(E; \gamma_i, \sigma, E_i, A_i) + B(E) \quad (\text{A.1})$$

where the i th Voigt is given by:

$$V_i(E; \gamma_i, \sigma, E_i, A_i) = \frac{A_i}{\sigma\sqrt{2\pi}} \int_{-\infty}^{\infty} \frac{\gamma_i e^{-x^2/(2\sigma^2)}}{\pi[(E - E_i - x)^2 + \gamma_i^2]} dx \quad (\text{A.2})$$

and γ_i is the Lorentzian broadening parameter (γ is the half-width half-maximum of the Lorentzian or $fwhm/2$), E_i is the centroid position and A_i is the integrated area of the Lorentzian. The Gaussian broadening parameter, σ , represents the common instrumental broadening.

The goodness of fit is characterised by χ_r^2 .

$$\chi_r^2 = \frac{\chi^2}{N_{\text{dof}}} \quad (\text{A.3})$$

where N_{dof} is the number of degrees of freedom.

The energy scale has been calibrated using [18], specifically the energies of the $K\beta_1$ and $K\beta_3$ components. The uncertainty in the number of counts in each channel of the detector was in our case very close to Poissonian ($\Delta I_i = \sqrt{I_i}$).

ORCID iDs

C T Chantler  <https://orcid.org/0000-0001-6608-0048>

References

- [1] Griem HR 1997 *Principles of Plasma Spectroscopy* (Cambridge Monographs on Plasma Physics) (Cambridge: Cambridge University Press)
- [2] Renner O and Rosmej F B 2019 Challenges of x-ray spectroscopy in investigations of matter under extreme conditions *Matter Radiat. Extremes* **4** 024201
- [3] Li X, Rosmej F B, Lisitsa V S and Astapenko V A 2019 An analytical plasma screening potential based on the self-consistent-field ion-sphere model *Phys. Plasmas* **26** 033301
- [4] Hansen S B *et al* 2005 Temperature determination using $K\alpha$ spectra from M -shell Ti ions *Phys. Rev. E* **72** 1–4
- [5] Šmíd M, Renner O, Colaitis A, Tikhonchuk V T, Schlegel T and Rosmej F B 2019 Characterization of suprathreshold electrons inside a laser accelerated plasma via highly-resolved K -emission *Nat. Commun.* **10** 1–8
- [6] Doniach S and Sunjic M 1970 Many-electron singularity in x-ray photoemission and x-ray line spectra from metals *J. Phys. C: Solid State Phys.* **3** 285–91
- [7] Armelao L, Bottaro G, Pascolini M, Sessolo M, Tondello E, Bettinelli M and Speghini A 2008 Structure-luminescence correlations in europium-doped sol–gel ZnO nanopowders *J. Phys. Chem. C* **112** 4049–54
- [8] Chantler C T, Kinnane M N, Su C and Kimpton J A 2006 Characterization of $K\alpha$ spectral profiles for vanadium, component redetermination for scandium, titanium, chromium, and manganese, and development of satellite structure for $Z = 21$ to $Z = 25$ *Phys. Rev. A* **73** 012508
- [9] Gillaspay J D, Chantler C T, Paterson D, Hudson L T, Serpa F G and Takács E 2010 First measurement of Lyman alpha x-ray lines in hydrogen-like vanadium: results and implications for precision wavelength metrology and tests of QED *J. Phys. B: At. Mol. Opt. Phys.* **43** 74021
- [10] Payne A T, Chantler C T, Kinnane M N, Gillaspay J D, Hudson L T, Smale L F, Henins A, Kimpton J A and Takacs E 2014 Helium-like titanium x-ray spectrum as a probe of QED computation *J. Phys. B: At. Mol. Opt. Phys.* **47** 185001
- [11] Smale L F, Chantler C T and Kimpton J A 2015 Methodology for the characterisation of characteristic spectral profiles, applied to chromium $K\beta$ X-Ray Spectrom. **44** 54–62
- [12] Dean J W, Melia H A, Chantler C T and Smale L F 2019 High accuracy characterisation for the absolute energy of scandium $K\alpha$ *J. Phys. B: At. Mol. Opt. Phys.* **52** 165002
- [13] Parratt L G 1936 $K\alpha$ satellite lines *Phys. Rev.* **50** 1–15
- [14] Berger H 1985 Study of the $K\alpha$ emission spectrum of copper *X-Ray Spectrom.* **15** 241–3
- [15] Sorum H 1987 The $K\alpha_{1,2}$ x-ray spectra of the 3d transition metals Cr, Fe, Co, Ni and Cu *J. Phys. F: Met. Phys.* **17** 417–25
- [16] Hartwig J, Holzer G, Wolf J and Forster E 1993 Remeasurement of the profile of the characteristic Cu $K\alpha$ emission line with high precision and accuracy *J. Appl. Crystallogr.* **26** 539–48
- [17] Deutsch M, Holzer G, Hartwig J, Wolf J, Fritsch M and Forster E 1995 $K\alpha$ and $K\beta$ x-ray emission spectra of copper *Phys. Rev. A* **51** 283
- [18] Hölzer G, Fritsch M, Deutsch M, Härtwig J and Förster E 1997 $K\alpha_{1,2}$ and $K\beta_{1,3}$ x-ray emission lines of the 3d transition metals *Phys. Rev. A* **56** 4554–68
- [19] Ito Y, Tochio T, Oohashi H and Vlaicu A M 2006 Contribution of the [1s3d] shake process to $K\alpha_{1,2}$ spectra in 3d elements *Radiat. Phys. Chem.* **75** 1534–7
- [20] Illig A J, Chantler C T and Payne A T 2013 Voigt profile characterization of copper $K\alpha$ *J. Phys. B: At. Mol. Opt. Phys.* **46** 235001
- [21] Mendenhall M H, Henins A, Hudson L T, Szabo C I, Windover D and Cline J P 2017 High-precision measurement of the x-ray Cu $K\alpha$ spectrum *J. Phys. B: At. Mol. Opt. Phys.* **50** 1–18
- [22] Melia H A, Chantler C T, Smale L F and Illig A J 2019 The characteristic radiation of copper $K\alpha_{1,2,3,4}$ *Acta Crystallogr. A* **75** 527–40
- [23] LaVilla R E 1979 Double-vacancy transitions in the copper $K\beta_{1,3}$ emission spectrum *Phys. Rev. A* **19** 717

- [24] Pham T L, Nguyen T V B, Lowe J A, Grant I P and Chantler C T 2016 Characterization of the copper $K\beta$ x-ray emission profile: an *ab initio* multi-configuration Dirac–Hartree–Fock approach with Bayesian constraints *J. Phys. B: At. Mol. Opt. Phys.* **49** 035601
- [25] Thomas T D 1984 Transition from adiabatic to sudden excitation of core electrons *Phys. Rev. Lett.* **52** 417–20
- [26] Enkisch H, Sternemann C, Paulus M, Volmer M and Schülke W 2004 3d spectator hole satellites of the Cu $K\beta_{1,3}$ and $K\beta_{2,5}$ emission spectra *Phys. Rev. A* **70** 022508
- [27] Heiser F, Whitfield S B, Viehhaus J, Becker U, Heimann P A and Shirley D A 1994 Threshold and near-threshold photoelectron spectroscopy around the Ar K edge *J. Phys. B: At. Mol. Opt. Phys.* **27** 19–31
- [28] Deutsch M, Gang O, Hämäläinen K and Kao K K 1996 Onset and near threshold evolution of the Cu $K\alpha$ x-ray satellites *Phys. Rev. Lett.* **76** 2424–7
- [29] Fritsch M, Kao C C, Hamalainen K, Gang O, Forster E and Deutsch M 1998 Evolution of the Cu $K\alpha_{3,4}$ satellites from threshold to saturation *Phys. Rev. A* **57** 1686–97
- [30] Galambosi S, Sutinen H, Mattila A, Hämäläinen K, Sharon R, Kao C C and Deutsch M 2003 Near-threshold multielectronic effects in the Cu $K\alpha_{1,2}$ x-ray spectrum *Phys. Rev. A* **67** 022510
- [31] Diamant R, Huotari S, Hämäläinen K, Sharon R, Kao C C and Deutsch M 2006 The evolution of inner-shell multielectronic x-ray spectra from threshold to saturation for low- to high- Z atoms *Radiat. Phys. Chem.* **75** 1434–46
- [32] Diamant R, Huotari S, Hämäläinen K, Sharon R, Kao C C and Deutsch M 2009 $K\alpha_{1,2}$ hypersatellites of 3d transition metals and their photoexcitation energy dependence *Phys. Rev. A* **79** 1–17
- [33] Aberg T and Utriainen J 1975 Interpretation of $KL_{2,3}L_{2,3}$ radiative Auger thresholds in metals and semiconductors *Solid State Commun.* **16** 571–3
- [34] Cao W *et al* 2011 High-resolution KMM radiative Auger x-ray emission spectra of calcium induced by synchrotron radiation *Phys. Rev. A* **83** 042513
- [35] Budnar M, Miihleisen A, Hribar M, Janiekovie H and Ravnikar M 1992 $K-MM$ radiative Auger effect in solid Ca, Ti and Cr targets after ionization with 0–745 MeV protons *Nucl. Instrum. Methods Phys. Res. B* **63** 377–83
- [36] Limandri S P, Carreras A C, Bonetto R D and Trincavelli J C 2010 $K\beta$ satellite and forbidden transitions in elements with $12 < Z < 30$ induced by electron impact *Phys. Rev. A* **81** 012504
- [37] Bearden J A and Burr A F 1967 Reevaluation of x-ray atomic energy levels *Rev. Mod. Phys.* **39** 125–42
- [38] Fuggle J C and Mårtensson N 1980 Core-level binding energies in metals *J. Electron Spectrosc. Relat. Phenom.* **21** 275–81
- [39] Chantler C T 1995 Theoretical form factor, attenuation, and scattering tabulation for $Z = 1-92$ from $E = 1-10$ eV to $E = 0.4-1.0$ MeV *J. Phys. Chem. Ref. Data* **24** 71–643
- [40] Deslattes R D, Kassler E G, Indelicato P, De Billy L, Lindroth E and Anton J 2003 X-ray transition energies: new approach to a comprehensive evaluation *Rev. Mod. Phys.* **75** 35–99
- [41] Kraft S, Stümpel J, Becker P and Kuetgens U 1996 High resolution x-ray absorption spectroscopy with absolute energy calibration for the determination of absorption edge energies *Rev. Sci. Instrum.* **67** 681–7
- [42] Larkins F P 1977 Semiempirical Auger-electron energies for elements $10 \leq z \leq 100$ *At. Data Nucl. Data Tables* **20** 311
- [43] Nigam A N and Soni S N 1981 Origin of low-energy satellites in k x-ray spectra II. β -region *J. Phys. C: Solid State Phys.* **14** 3289
- [44] Seetharami Reddy B, Ram Narayana K, Abdul Sattar S and Koteswara Rao V 2019 KMM RAE structure and Sawada lines of Co, Ni, Cu, Zn and Ga *Nucl. Instrum. Methods Phys. Res. B* **448** 43–51
- [45] Keski-Rahkonen O and Ahopelto J 1980 The K to M radiative Auger effect in transition the $K - + M_2$ radiative Auger effect in transition metals II *J. Phys. C: Solid State Phys.* **13** 471–82
- [46] Kawai J, Nakajima T, Inoue T, Adachi H, Yamaguchi M, Maeda K and Yabuki S 1994 Chemical effects on the intensity of Ti $K\eta$ (radiative Auger satellite) x-ray fluorescence spectra *Analyst* **119** 601–3
- [47] Kawai J, Hayashi K and Awakura Y 1997 Extended x-ray absorption fine structure (EXAFS) in x-ray fluorescence spectra *J. Phys. Soc. Japan* **66** 3337–40
- [48] Hayashi K, Kawai J and Awakura Y 1997 Extended fine structure in characteristic x-ray fluorescence: a novel structural analysis method of condensed systems *Spectrochim. Acta B* **52** 2169–72
- [49] Abrahams I, Kövér L, Tóth J, Urch D S, Vrebos B and West M 2001 Absorption in emission: radiative Auger spectra in silica, phosphate and sulfate *J. Electron Spectrosc. Relat. Phenom.* **114–116** 925–31
- [50] Kawai J, Hayashi K and Tanuma S 1998 Extended x-ray emission fine structure of sodium *Analyst* **123** 617–9
- [51] Kawai J, Takahashi H, Hayashi K, Okazaki S and Awakura Y 1999 Magnesium K x-ray emission spectra of Mg, MgO and olivine [(Mg, Fe) $_2$ (SiO $_4$)] by EPMA and XRF *Tetsu-to-Hagane* **85** 164–8
- [52] Tanuma S and Nishio M 1998 Al K -edge extended fine structures in x-ray emission spectra of aluminium metal and aluminium oxide measured by an electron probe microanalyzer (EPMA) *Spectrochim. Acta B* **53** 505–7
- [53] Kawai J and Takahashi H 1999 Si x-ray absorption near edge structure (XANES) of Si, SiC, SiO $_2$, and Si $_3$ N $_4$ measured by an electron probe x-ray microanalyzer (EPMA) *Spectrochim. Acta B* **54** 231–4
- [54] Fujikawa T and Kawai J 1999 Theory on extended x-ray emission spectra *J. Phys. Soc. Jpn.* **68** 4032–6
- [55] Kawai J 1999 Theory of radiative Auger effect—an alternative to x-ray absorption spectroscopy *J. Electron Spectrosc. Relat. Phenom.* **101–103** 847–50
- [56] Scofield J H 1969 Radiative decay rates of vacancies in the K and L shells *Phys. Rev.* **179** 9–16
- [57] Rosner H R and Bhalla C P 1970 Relativistic calculation of atomic x-ray transition rates *Z. Phys. A* **231** 747–811
- [58] Lu C C, Malik F B and Carlson T A 1971 Calculation of the K x-ray intensities for elements from $Z = 92$ to 126 *Nucl. Phys. A* **175** 289–99
- [59] Salem S I, Panossian S L and Krause R A 1974 Experimental K and L relative x-ray emission rates *At. Data Nucl. Data Tables* **14** 91–109
- [60] Berenyi D, Hock G, Ricz S, Schlenk B and Valek A 1978 $K\alpha/K\beta$ x-ray intensity ratios and K -shell ionisation cross sections for bombardment by electrons of 300–600 keV *J. Phys. B: At. Mol. Phys.* **11** 709–13
- [61] Scofield J 1974 Exchange corrections of K x-ray emission rates *Phys. Rev. A* **9** 1041–9
- [62] Campbell J L, Perujo A and Teesdale W J 1986 $K\alpha$, $K\beta$, and radiative Auger photon intensities in K x-ray spectra from atoms in the $20 \leq Z \leq 40$ region *Phys. Rev. A* **33** 2410–7
- [63] Lépy M C, Plagnard J and Morel J 1994 Radiative Auger effect: an explanation for discrepancies between theoretical and experimental emission probability ratios? *Nucl. Instrum. Methods Phys. Res. A* **339** 241–7
- [64] Bé M-M, Lepy M-C, Plagnard J and Duchemin B 1998 Measurement of relative x-ray intensity ratios for elements in the $22 \leq Z \leq 29$ region *Appl. Radiat. Isot.* **49** 1367–72
- [65] Kavcic M, Budnar M, Muhleisen A and Torok I 1998 High resolution study of the K x-ray spectra from low Z elements *Nucl. Instrum. Methods Phys. Res. B* **138** 173–8

- [66] Herren C and Dousse J-C 1996 High-resolution measurements of the K - MM radiative Auger effect in medium-mass atoms *Phys. Rev. A* **53** 717–25
- [67] Lépy M C, Bé M M and Plagnard J 1997 Processing of x-ray spectra using a peak shape calibrated Si(Li) detector *AIP Conf. Proc.* **392** 1067–70
- [68] Baptista G B 2001 K - MM radiative-Auger transition probability calculations for Ca, Ti and Cr *J. Phys. B: At. Mol. Opt. Phys.* **34** 389–404
- [69] Krause M O and Oliver J H 1979 Natural widths of atomic K and L levels, $K\alpha$ x-ray lines and several KLL Auger lines *J. Phys. Chem. Ref. Data* **8** 329–38
- [70] Cipolla S J 1999 K x-ray production cross sections, $K\beta/K\alpha$, and radiative Auger ratios for protons impacting low- Z elements *Nucl. Instrum. Methods Phys. Res. A* **422** 546–50
- [71] Servomaa A and Keski-Rahkonen O 1975 K to M^2 radiative Auger effect in transition metals. I *J. Phys. C: Solid State Phys.* **8** 4124
- [72] Cengiz E, Biyiklioğlu Z, Aylikci N K, Aylikci V, Apaydin G, Tiraolu E and Kantekin H 2010 Chemical effect on K shell x-ray fluorescence parameters and radiative auger ratios of Co, Ni, Cu, and Zn complexes *Chin. J. Chem. Phys.* **23** 138–44
- [73] Melia H A, Dean J W, Chantler C T, Smale L F and Illig A J 2019 Count-rate, linearity, and performance of new backgammon detector technology *X-Ray Spectrom.* **48** 218–31
- [74] Markwardt C B 2009 Non-linear least-squares fitting in idl with mpfit *Astronomical Data Analysis Software and Systems XVIII* (Astronomical Society of the Pacific Conference Series vol 411) ed D A Bohlender, D Durand and P Dowler p 251
- [75] Tsutsumi K 1959 The x-ray non-diagram lines $K\beta'$ of some compounds of the iron group *J. Phys. Soc. Jpn.* **14** 1696–706
- [76] Srivastava K S, Singh S, Srivastava A K, Nayal R S, Chaubey A and Gupta P 1982 Electron–electron interaction in transition-metal x-ray emission spectra *Phys. Rev. A* **25** 2838–44
- [77] Mandić L, Fazinić S and Jakšić M 2009 Chemical effects on the $K\beta''$ and $K\beta_{2,5}$ x-ray lines of titanium and its compounds *Phys. Rev. A* **80** 1–10
- [78] Salem S and Wimmer R 1970 $K\alpha_2/K\alpha_1$ transition probabilities in elements with $Z < \approx 50$ *Phys. Rev. A* **2** 1121–3
- [79] Koster A and Mendel H 1970 X-ray $K\beta$ emission spectra and energy levels of compounds of 3D-transition metals II. Non-oxidic compounds *J. Phys. Chem. Solids* **31** 2523–30
- [80] Antonides E, Jose E C and Sawatzky G A 1977 LMM Auger spectra of Cu, Zn, Ga, and Ge I. Transition probabilities, term splitting, and effective Coulomb interaction *Phys. Rev. B* **15** 1669–79
- [81] Schön G 1972 High resolution Auger electron spectroscopy of metallic copper *J. Electron Spectrosc. Relat. Phenom.* **1** 377–87
- [82] Chantler C T, Hayward A C L and Grant I P 2009 Theoretical determination of characteristic x-ray lines and the copper $K\alpha$ spectrum *Phys. Rev. Lett.* **103** 2–5
- [83] Chantler C T, Lowe J A and Grant I P 2010 Multiconfiguration Dirac–Fock calculations in open-shell atoms: convergence methods and satellite spectra of the copper $K\alpha$ photoemission spectrum *Phys. Rev. A* **82** 0–3
- [84] Campbell J L and Papp T 2001 Widths of the atomic $K-N7$ levels *At. Data Nucl. Data Tables* **77** 1–56
- [85] Obert L and Bearden J A 1938 The effect of chemical combination on K fluorescent x-ray emission lines *Phys. Rev.* **54** 1000–4
- [86] Edamoto I 1950 The fine structure of K -series x-ray emission spectra of the elements Mn(25)–Zn(30) and Ge(32)* *Sci. Rep. Res. Inst. Tokohu Univ. A* **2** 561–612